Bioactive Materials 31 (2024) 231–246

Contents lists available at ScienceDirect

Bioactive Materials

journal homepage: www.keaipublishing.com/en/journals/bioactive-materials

Ultrasound-triggered biomimetic ultrashort peptide nanofiber hydrogels promote bone regeneration by modulating macrophage and the osteogenic immune microenvironment

Fan Zhang [a,1], Mingchen Lv [b,c,1], Siyuan Wang [a], Mengyao Li [d], Yu Wang [a], Congjiao Hu [a], Wei Hu [b,c], Xuekui Wang [a], Xiaogang Wang [e], Zhiduo Liu [d], Zhen Fan [b,c,***], Jianzhong Du [b,c,*], Yao Sun [a,**]

[a] Department of Oral Implantology, Stomatological Hospital and Dental School of Tongji University, Shanghai Engineering Research Center of Tooth Restoration and Regeneration, 200072, China
[b] Department of Gynaecology and Obstetrics, Shanghai Fourth People's Hospital, School of Medicine, Tongji University, Shanghai, 200434, China
[c] Department of Polymeric Materials, School of Materials Science and Engineering, Tongji University, 201804, China
[d] Department of Immunology and Microbiology, The Minister of Education Key Laboratory of Cell Death and Differentiation, Shanghai Institute of Immunology, Shanghai Jiao Tong University School of Medicine, China
[e] Key Laboratory of Big Data-Based Precision Medicine, School of Engineering Medicine, Beihang University, China

ARTICLE INFO

Keywords:
Peptide
Nanofiber hydrogel
Immune microenvironment
Bone tissue regeneration

ABSTRACT

The immune microenvironment plays a vital role in bone defect repair. To create an immune microenvironment that promotes osteogenesis, researchers are exploring ways to enhance the differentiation of M2-type macrophages. Functional peptides have been discovered to effectively improve this process, but they are limited by low efficiency and rapid degradation *in vivo*. To overcome these issues, peptide with both M2 regulatory and self-assembly modules was designed as a building block to construct an ultrasound-responsive nanofiber hydrogel. These nanofibers can be released from hydrogel in a time-dependent manner upon ultrasound stimulation, activating mitochondrial glycolytic metabolism and the tricarboxylic acid cycle, inhibiting reactive oxygen species production and enhancing M2 macrophage polarization. The hydrogel exhibits advanced therapeutic potential for bone regeneration by triggering M2 macrophages to secrete BMP-2 and IGF-I, accelerating the differentiation of bone marrow mesenchymal stem cells (BMSCs) into osteoblasts. Thus, modularly designed biomimetic ultrashort peptide nanofiber hydrogels provide a novel strategy to rebuild osteogenic immune microenvironments for bone repair.

1. Introduction

Achieving ideal bone defect repair remains a significant challenge for patients with trauma, tumor resection, atrophic nonunion and etc. [1] The regenerative microenvironment of bone defects relies on stem cells, extracellular matrix (Extracellular Matrix, ECM), secreted bioactive factors [2], whose interactions between each other form bone-specific microenvironment [3]. With the development of bone immunology, more and more studies have shown that the process of bone regeneration is not simply a process of bone formation and resorption, but a close interplay of multiple systems, including the skeletal system and the immune system [4]. Immune cells, which secrete factors to establish microenvironments that regulate osteoblast and osteoclast differentiation [5], play a crucial regulatory role in bone formation and resorption. Macrophages, important components of the innate immune system, exhibit remarkable flexibility and can convert to proinflammatory M1

Peer review under responsibility of KeAi Communications Co., Ltd.
* Corresponding author. Department of Polymeric Materials, School of Materials Science and Engineering, Tongji University, 201804, China.
** Corresponding author.
*** Corresponding author. Department of Gynaecology and Obstetrics, Shanghai Fourth People's Hospital, School of Medicine, Tongji University, Shanghai, 200434, China.
E-mail addresses: fanzhen2018@tongji.edu.cn (Z. Fan), jzdu@tongji.edu.cn (J. Du), yaosun@tongji.edu.cn (Y. Sun).
[1] These authors contributed equally to this work.

https://doi.org/10.1016/j.bioactmat.2023.08.008
Received 26 May 2023; Received in revised form 28 July 2023; Accepted 8 August 2023

macrophages or reparative M2 macrophages depending on the molecular mediators present in the microenvironment [6]. M2-type macrophages ultimately play a vital anti-inflammatory regulatory role by releasing paracrine cytokines such as BMP2, TGF-β, IGF-I and exosomes, secreting cytokines to promote stem cell differentiation and tissue regeneration [7]. Therefore, regulating M2-type macrophage polarization to establish a beneficial immune microenvironment for injury repair has become a key challenge in the field of bone regeneration.

To date, methods utilized to regulate the polarization of M2 macrophages chiefly include biologically active agents, immunomodulators, and chemokines [7b-d]. Nonetheless, continuous regulation of macrophages is essential for bone defect repair but not been achieved, due to a dearth of safe and effective functional molecules that can be utilized over an extended period and difficulties in achieving controlled local release[[4a,8]]. Therefore, identification of novel functional strategies that can effectively regulate M2-type macrophage polarization to modify the immune microenvironment and stimulate bone regeneration is urgently needed. Ultrashort peptides exhibit superior biological function, higher safety, and lower synthesis costs than other biomolecules [9]. However, natural peptides may not always be appropriate as therapeutics because of their inherent weaknesses, such as short half-life, unstable physicochemical properties, and rapid hydrolysis. Developing immunomodulatory peptides with clinical translation potential, including excellent drug-forming abilities, antidegradation properties, and biological safety, is consequently crucial. Oligopeptides of no more than eight are often referred to as ultrashort peptides, which have received a wide attention recently. Accordingly, our goal was to develop an ultrashort peptide system capable of modulating the immune microenvironment of bone defects to expedite osteogenesis and promote bone damage regeneration.

Recently, bioactive materials have garnered widespread attention as functional molecules and have gradually been adopted for biomedical use, including in the treatment of immunodeficiency-related illnesses, accelerated osteogenic differentiation of mesenchymal stem cells, improved tissue vascularization, and promotion of nerve regeneration [10]. In this study, we designed an ultrashort peptide (Ser-Glu-Ser-Ser-Glu, SESSE) with the ability to promote M2 type macrophage polarization and BMSC differentiation (Scheme 1). To enhance *in vivo* stability, we modularly designed the SESSE peptide with an assembly module (CFF, yellow) and an M2 polarization module (SESSE, green), which could self-assemble into nanofibers. Additionally, we synthesized an ultrasound-responsive hydrogel *in situ* with self-assembled ultrashort peptide nanofibers (denoted as UPN@hydrogel) for repairing three-dimensional spatial defects caused by bone injuries. The ultrasound-triggered hydrogel was formed by the coordination between the carboxyl group of alginate and calcium ions [11], and the disruption of the coordination between the calcium ions and the carboxyl group under sonication led to the degradation of the hydrogel, which promoted the release of the encapsulated nanofibers [12]. Meanwhile, UPN@hydrogel served as a stable and deformable three-dimensional scaffold to fill in the bone defect region. As a result, the controlled release of active ultrashort peptide nanofibers was able to enhance the osteogenic immune microenvironment and promoted bone repair, which could provide a novel strategy for clinical bone defect repair.

2. Results

2.1. Synthesis and characterizations of UPN@hydrogel

First, peptide nanofibers were prepared through the self-assembly of CFF-SESSE, as illustrated in Scheme 1. As shown in Fig. 1A, crosslinked nanofiber network was observed in SEM (Scanning Electron Microscope) image. Then, calcium alginate hydrogel was synthesized *in situ* alongside nanofibers as UPN@hydrogel. To verify the successful synthesis of such peptide nanofiber hydrogels, FITC-labeled peptide nanofibers were fabricated in advance. As shown in Fig. 1B, a uniform distribution of green fluorescence was observed, confirming the uniform distribution of peptide nanofibers within the hydrogel. In addition, the FITR results (Fig. S1) showed that there was shift from 1495.5 cm^{-1} to 1485.8 cm^{-1}, indicating the coordination between the carboxyl group of alginate and calcium ions to verify the formation of calcium alginate hydrogel [13].

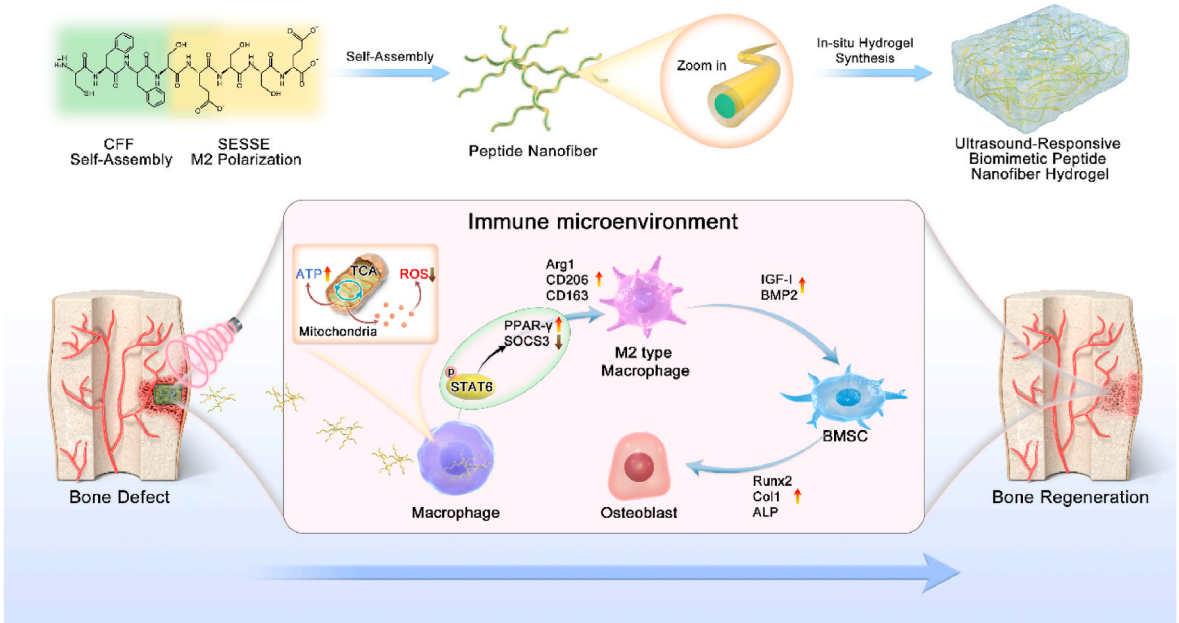

Scheme 1. Ultrashort peptides were modularly self-assembled into nanofiber hydrogels with the role of mediating M2 polarization to promote bone defect regeneration. Ultrashort peptides were self-assembled to form nanofibers. To fill the bone defect space, the ultrashort peptide-formed nanofibers were loaded into calcium alginate hydrogels with ultrasound trigger. Upon ultrasound stimulation at the bone defect site, the ultrashort peptide nanofibers were responsively released from the hydrogel. The ultrashort peptide nanofibers not only inhibited reactive oxygen species production by activating oxidative stress in macrophage mitochondria but also accelerated osteogenic differentiation of bone marrow mesenchymal stem cells by inducing M2 macrophage polarization and promoting paracrine secretion of BMP-2 and IGF-I from M2 macrophages, which was achieved via the STAT6/PPAR-γ/SOCS3 signaling axis.

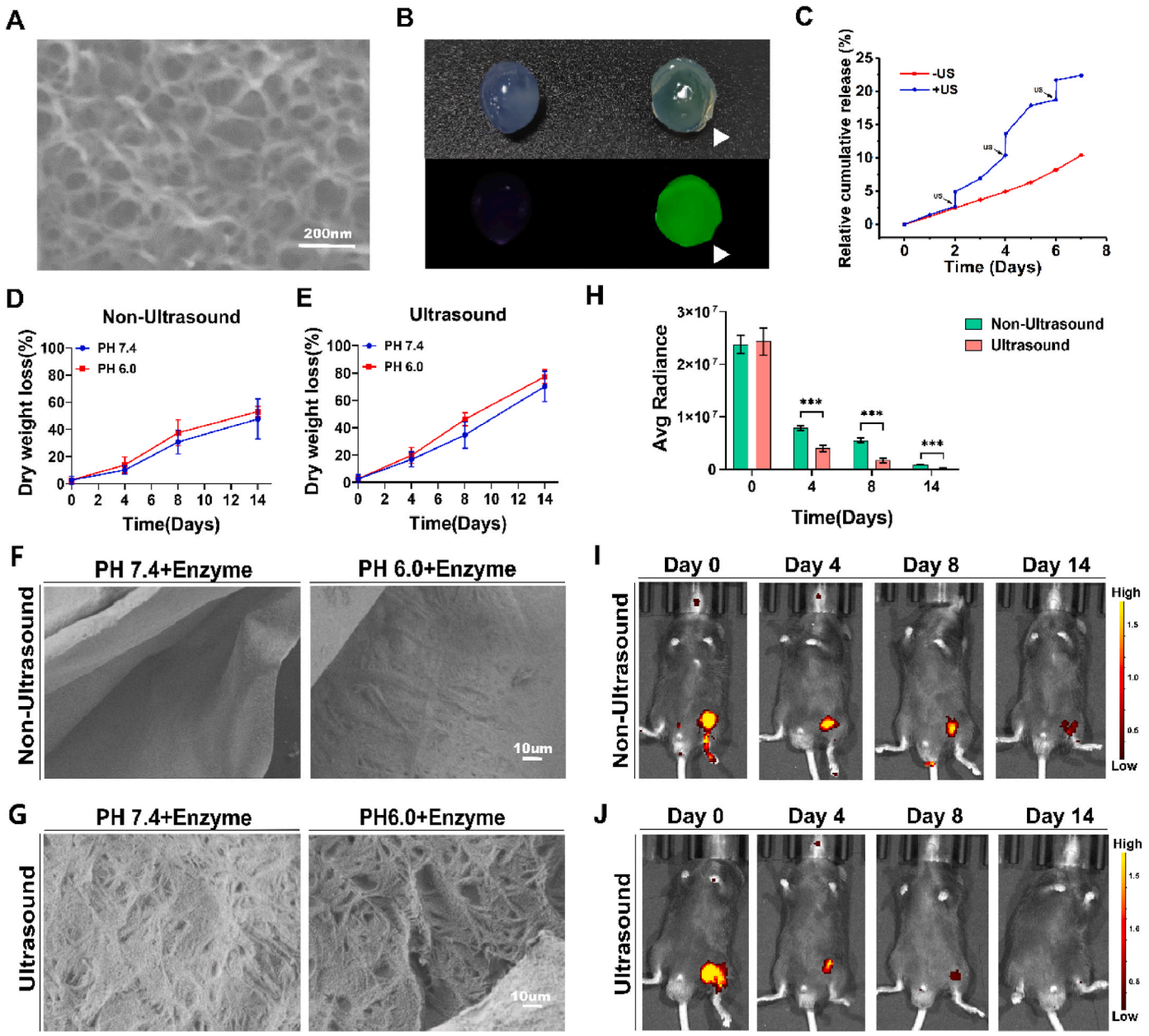

Fig. 1. Morphological characterizations and ultrasound responsiveness evaluation of UPNs. (A) SEM images of the peptide nanofibers. (B) Optical images of the hydrogel and FITC-peptide nanofiber-loaded hydrogel. (C) Cumulative release of peptide nanofibers from the hydrogels with or without sonication over 7 days. (D–E) Degradation profiles of the hydrogels after incubation under different conditions over 14 days with or without ultrasound. n = 5. (F–G) SEM of the ultrashort peptide nanofiber hydrogels in different culture environments with non-ultrasound/ultrasound. (H) Quantitative analysis of hydrogel degradation in bone defects, n = 4. (I–J) Degradation images of hydrogels in bone defects over 14 days with or without sonication. **: $P < 0.01$.

Meanwhile, loading efficiency and loading content of peptide nanofibers within hydrogels were 45.2 ± 1.4% and 10.5 ± 0.5%, respectively (Fig. S2). Also, rheological analysis was applied to confirm the rheological properties of the hydrogels, the results showed both high storage modulus (G') and high loss modulus (G") values, indicating stiff hydrogels that are suitable for bone defect filling (Fig. S3). Furthermore, the stress-strain curve of the hydrogels with different contents of peptide nanofiber was measured (Fig. S4), demonstrating that hydrogels with peptide nanofiber loading were weaker in compressive strength compared to calcium alginate hydrogels, which was also suitable to fill the bone defect site.

2.2. Evaluating the ultrasound responsiveness of UPN@hydrogel

Firstly, the degradation behavior of hydrogels under varying sonication strengths was studied. In addition, ultrasound triggered accelerated release of UPN@hydrogel was also observed as shown in Fig. 1C. Upon termination of ultrasound stimulation, the hydrogel continued to release peptide nanofibers in a sustained manner. Besides, UPN@hydrogel was immersed in PBS solution (pH 6.0 and 7.4) to mimic the acidic microenvironment in bone defected area, and the ultrasonic reaction still accelerated the loss of hydrogel weight (Fig. 1D and E). Moreover, various parameters of ultrasound were also applied here: no sonication treatment, 1 W/cm^2, 1.75 W/cm^2 and 2.5 W/cm^2 sonication for 2 min. The results showed that, as the sonication intensity increased, degradation rate of the hydrogels was also accelerated (Fig. S5).

Similarly, more cavities were observed of UPN@hydrogel upon applied ultrasound (Fig. 1F and G). Also, there was no significant difference between the hydrogels with and without trypsin, demonstrating desired stability against trypsin (Fig. S6). Besides *in vitro* study, *in vivo* kinetics of hydrogel degradation in bone defects without (Fig. 1I) or with (Fig. 1J) ultrasound was also studied by whole body fluorescent imaging, which quantitatively showed that the ultrasound response accelerated the degradation of the hydrogel (Fig. 1H).

2.3. Modulating macrophage mitochondrial metabolism and oxidative stress by UPNs

The phagocytosis of ultrashort peptide nanofibers by macrophages was first studied by immunofluorescence. The results showed that UPNs began to be engulfed by macrophages at 6 h, with increasing incubation time and increasing stimulation concentration of UPN, UPNs were increasingly engulfed by macrophages (Fig. 2A). However, the ultrashort peptide nanofibers were not significantly engulfed by BMSCs (Fig. 2B). Mitochondrial metabolism is a key controller of the functional transformation of macrophages and determines their polarization state [14]. Metabolomic analysis of macrophages showed that macrophages cultured with UPNs were closely associated with glycolysis (EMP) and the tricarboxylic acid cycle (TCA), suggesting that UPNs could activate the glycolysis and tricarboxylic acid cycle of macrophages (Fig. 2C–E). Quantitative analysis succinic acid in the TCA cycle showed that UPNs suppressed succinic acid metabolism (Fig. 2F). Simultaneously, quantitative analysis of lactic acid and glucose 6 phosphate in EMP metabolism showed that UPNs reduced the production of lactic acid (Fig. 2G) and glucose 6 phosphate in macrophages (Fig. 2H). TEM was used to detect the morphology of the mitochondria in macrophages, revealing that UPNs induced the morphology of mitochondria to change from an original baseball-like morphology to an expanded oval state (Fig. 2I). After incubation of macrophages with UPs and UPNs, we found that the percentage of swollen mitochondria was 53% in the UPN group, 38% in the UP group and nearly 20% in the Ctrl group, and the proportion of swollen mitochondria in the UPN group was further increased compared with that in the Ctrl group (Fig. 2J). In addition, the ratio of mitochondria/cell result showed that the ratio in the UPN group was further increased compared to that in the Ctrl group (Fig. 2K). The effects of UPN on the mitochondrial structure of macrophages were analyzed using mitochondrial membrane potential and the release of reactive oxygen species (Reactive Oxygen Species, ROS). JC-1 was used to detect mitochondrial membrane potential JC-1. Immunofluorescence results revealed that UPN could increase the expression of JC-1 polymer from 0.02 fluorescence intensity in the control group to 0.13 in the UPN group (Fig. 2L-M). ATP testing showed that UPNs promoted the tricarboxylic acid cycle in macrophage mitochondria, indicating that macrophage energy metabolism was activated (Fig. 2N). In flow cytometry analysis, total ROS in macrophages were labeled with DCGH-DA (Fig. 2O), and the ROS in mitochondria were labeled with MitoSox (Fig. 2P). The results showed that UPNs were able to reduce not only total ROS release in macrophages but also the release of ROS in the mitochondria of macrophages (Fig. 2Q-R). In summary, UPNs could regulate mitochondrial metabolism, enhance MMP activity and reduce ROS release.

2.4. Promoting the polarization of M2-type macrophages by UPNs

M1 proinflammatory macrophages and M2 repair macrophages have been reported to affect tissue regeneration after injury [15]. Arg1, CD206, and CD163 are genes expressed by M2-type macrophages. Gene transcript sequencing analysis of bone defects in mice treated with UPs for 14 days showed a marked increase in the expression of Arg1 and CD163 (Fig. 3A). After 14 days of ultrasound treatment with ultrashort peptide nanofiber hydrogel (denoted as US + UPN@hydrogel) in the bone defect area, M2-type macrophages were labeled with F4/80 and CD206 (Fig. 3B and C). Flow cytometry showed an increase in the number of CD206-labeled M2-type macrophages as a percentage of the total macrophage population (Fig. 3D), whereas CD86-labeled M1-type macrophages showed no significant difference (Fig. 3E). Immunofluorescence results showed that US + UPN@hydrogel was able to increase the expression of CD206 at the bone defect (Fig. 3F). To reveal the interaction between biomimetic peptide nanofibers and macrophages, we incubated IL-4 with BMDMs to study the M2-type macrophage polarization *in vitro*, immunofluorescence showed that UPNs were able to further promote IL-4-mediated expression of the M2-type macrophage markers Arg1 and CD206 (Fig. 3G–I). Flow cytometry was used to test the expression of CD163 and CD206 (Fig. 3J and K), and the results showed that the expression of CD163 was 70.6% in the IL-4+UPN group, 50.3% in the IL-4 group and nearly 17.2% in the Ctrl group (Fig. 3L). In addition, the expression of CD206 was 61.8% in IL-4+UPN group, 40.9% in IL-4 group and nearly 18.1% in the Ctrl group (Fig. 3M). RT−qPCR results showed that UPNs significantly increased the expression of Arg1 and CD206 (Fig. 3N-O). Similarly, the Western blot results showed that UPNs obviously promoted Arg1 and CD206 protein expression (Fig. 3P). In summary, these findings suggested that M2 repair macrophages played a leading role during bone defect regeneration after UPN@hydrogel treatment, and the ultrasound trigger further promoted the polarization of M2-type macrophages.

2.5. Modulating the STAT6/PPAR-γ/SOCS3 axis by UPNs to induce the polarization of M2-type macrophages

Preliminary findings of the team, bone defects in mice were treated with tail vein injection of UPs for 14 days, Gene Ontology analysis, Kyoto Encyclopedia of Genes and Genomes analysis and Gene Set Enrichment analysis revealed that UPs were closely related to the JAK/STAT signaling pathway (Fig. 4A–C). To confirm the molecular mechanism of UPN-induced polarization of M2 type macrophages, we induced M2-type macrophages with IL-4 and UPNs for 24 h, which had significantly increased p-STAT6 fluorescence intensity compared to that of the Ctrl group (Fig. 4D). Semiquantitative analysis revealed that the addition of UPN in IL-4+UPN group (13.5%) significantly enhanced the p-STAT6 fluorescence intensity compared with that in the IL-4 group (7.8%) and Ctrl group (1.7%) (Fig. 4E). Western blotting results confirmed that the addition of UPN to M2-type macrophages resulted in increased levels of p-STAT6 and PPAR-γ proteins and decreased levels of SOCS3 protein, indicating that UPN further promoted M2 macrophage polarization by enhancing STAT6 and PPAR-γ proteins, and that UPN mediated a decrease in SOCS3 protein to promote M2-type macrophage polarization (Fig. 4F). Notably, in the IL-4+UPN group, the p-STAT6 and PPAR-γ protein concentrations increased markedly, while the SOCS3 protein concentration decreased significantly. However, there was no significant difference in SOCS3, p-STAT6 or PPAR-γ expression between the UPN group and Ctrl group. The above findings suggested that the UPNs further induced M2-type macrophage polarization via the STAT6/PPAR-γ/SOCS3 signaling axis (Fig. 4F). Flow cytometry results showed that GW9662 (PPAR-γ inhibitor) inhibited UPN-induced expression of the M2 type macrophage marker CD206 (Fig. 4G). Flow cytometry results showed that STAT6-IN-1 (STAT6 inhibitor) inhibited UPN-induced expression of the M2-type macrophage marker CD206 (Fig. 4H).

2.6. Promoting the osteogenic differentiation and migration of BMSCs by UPNs

BMSCs are seed cells capable of bone damage regeneration [16]. Studies have shown that the transformation of macrophages from the proinflammatory M1 subtype to the anti-inflammatory M2 subtype plays a vital role during bone damage regeneration because cytokines secreted by macrophages have a significant impact on stem cell recruitment, proliferation and differentiation [17]. To further verify whether paracrine growth factors from M2 macrophages influence the behavior and fate of BMSCs, we used coculture systems to evaluate the

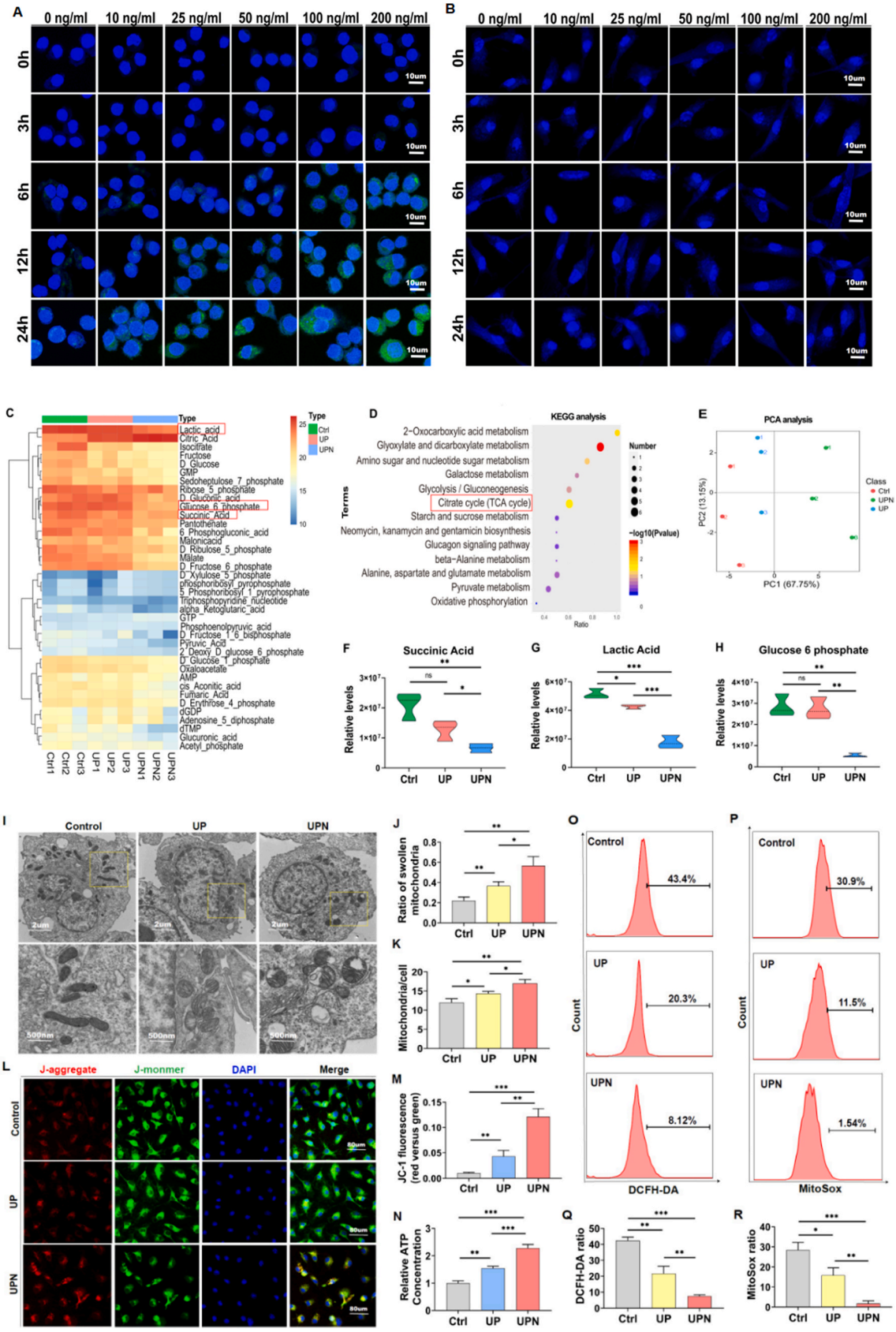

(caption on next page)

Fig. 2. Study of macrophage mitochondrial metabolism and oxidative stress induced by UPNs. (A) UPNs were engulfed in macrophages from 6 to 24 h with stimulation concentrations of 10–200 ng/ml (B) UPNs were not engulfed enough by BMSCs from 6 to 24 h with stimulation concentrations of 10–200 ng/ml. (C) Metabolomic analysis of UP- and UPN- induced macrophages. (D) KEGG analysis of UP- and UPN- induced macrophages. (E) PCA of UP- and UPN- induced macrophages. (F) Quantitative analysis of succinic acid in the TCA cycle. G-H) Quantitative analysis of lactic acid and glucose 6 phosphate in glycolysis metabolism. (I) Transmission electron microscopy images (TEM) of UP and UPN induced macrophages. (J) Quantitative analysis of the ratio of expanded mitochondria to the total number of mitochondria. (K) Quantitative analysis of the ratio of mitochondria to the total number of macrophages. (L) JC-1 immunofluorescence staining to detect the content of metalloproteinases (MMPs) in the macrophage matrix. (M) Quantitative analysis of the ratio of red fluorescence intensity to green fluorescence intensity to determine the content of MMPs in macrophages. (N) ATP detection quantitatively showed the release of macrophage adenosine triphosphate. (O) DCFH-DA fluorescent probe detection after UP and UPN stimulation to evaluate the content of ROS in macrophages. (P) MitoSox fluorescent probe detection after UP and UPN stimulation to evaluate the content of ROS in mitochondria. (Q) Flow cytometry to quantitatively analyze the ROS content in macrophages. (R) Quantitative analysis of ROS content in mitochondria by flow cytometry. Quantitative data for cell experiments are shown as the mean ± SD (n = 3). *: $P < 0.05$; **: $P < 0.01$; ***$p < 0.001$.

interaction between BMDMs and BMSCs. A schematic diagram of the coculture of UPN-treated BMDMs and BMSCs is shown in (Fig. 5A). Alkaline phosphatase staining was performed to detect the osteogenic mineralization of BMSCs, and it was found that the activity of BMSC alkaline phosphatase in the IL-4+UPN group was significantly increased compared with that in the Ctrl group on days 7 (Fig. 5B and C) and 14 (Fig. 5D and E) in the coculture system. Moreover, alizarin red staining showed that the number of mineralized nodules in BMSCs in the IL-4+UPN group increased compared with that in the Ctrl group on day 21 in the coculture system (Fig. 5F and G). The above results proved that the ultrashort peptide nanofibers could further induce the polarization of macrophages into the M2 subtype. Therefore, after UPN-induced M2 macrophage polarization, the paracrine effects of growth factors from M2 macrophages promoted the osteogenic differentiation of BMSCs.

To further investigate the paracrine effect of macrophages of the M2 subtype on BMSCs, we assessed the migration capacity of BMSCs in a coculture system. Transwell migration experiments showed that there were no significant differences in BMSCs among the Ctrl group, IL-4 group and IL-4+UPN group at 0 h (Fig. 5H). The percentage of migrating cells was 18.5% in the IL-4+UPN group, 7.2% in the IL-4 group and nearly 2% in the control group at 24 h (Fig. 5I). The addition of UPN to the IL-4+UPN group (23.6%) significantly enhanced the number of migrating cells compared with that in the IL-4 group (13.7%) and the control group (4.8%) at 48 h (Fig. 5J). The above results suggested that UPNs effectively facilitated the migration of BMSCs. RT–qPCR was used to detect osteogenesis-related genes in BMSCs, including alkaline phosphatase (ALP) and Runt-related transcription factor 2 (Runx2), and the results showed that ultrashort peptide nanofibers could significantly improve the osteogenic differentiation of BMSCs (Fig. 5K-L). In addition, bone morphogenetic protein-2 (BMP-2) and insulin-like growth factors (IGF-1) are growth factors secreted by macrophages [18]. We hypothesised that UPNs could act on BMSCs by paracrine secretion of IGF-1 growth factor (Fig. 5M − N).

2.7. Effect of the ultrasound-responsive UPN@hydrogel in the treatment of bone defects in vivo

SPF-grade 8-week-old C57BL/6J mouse bone defect model was constructed, and the bone defect was subjected to ultrasound-triggered UPN@hydrogel (Fig. 6A). To visualize the healing process, micro-CT imaging was used to examine the healing effect of bone defects in different groups. At 14 days after surgery, micro-CT reconstructed images (Fig. 6B) of the bone defect sites, and X-ray images (Fig. 6C) were obtained. Micro-CT scans were performed to quantitatively analyze bone volume/tissue volume (BV/TV) and trabecular thickness (Tb. Th) in the healing area of bone defects. The results showed that the US + UPN@hydrogel group had a better bone healing effect (Fig. 6D and E). Furthermore, protein extraction from tissue at the site of the bone defect and western blotting showed that the US + UPN@ hydrogel group had the highest levels of the osteogenic protein markers BMP2 and Col1 (Fig. 6F). H&E staining was used to evaluate the healing ability of mouse bone defects, revealing that the newly formed trabeculae were gradually replaced by newly regenerated bone in the bone defect area of mice (Fig. 6G). Immunofluorescence detection of the osteogenesis gene marker BMP2 revealed red fluorescence, and the US + UPN@hydrogel group had the strongest fluorescence intensity compared to the Ctrl group (Fig. 6H). These findings confirmed that the application of an ultrasound-triggered ultrashort peptide nanofiber hydrogel material could effectively improve the regeneration of bone defects.

2.8. In vivo toxicity study of UPN@hydrogel

In this study, we conducted local placement of the UP@hydrogel (denoted as US + UP@hydrogel) and UPN@hydrogel (denoted as US + UPN@hydrogel) within mouse bone defect areas. The UP@hydrogel referred to a monomeric peptide hydrogel, while the UPN@hydrogel referred to an assembled peptide nanofiber hydrogel. Ultrasound stimulation was utilized to trigger the therapeutic response of these hydrogels. After 14 days of treatment, the drug toxicity in the heart, liver, spleen, lung and kidney was examined using H&E staining, which showed no inflammatory infiltration or pathological changes in these organs (Fig. 7A). In our study, we performed *in vivo* assessments to evaluate the safety of UPN@hydrogel. Serum samples were carefully extracted to investigate potential alterations in liver, kidney, and heart function, as well as the inflammatory response. To comprehensively analyze the safety profile of UPN@hydrogel, we conducted thorough evaluations on the extracted serum samples. Our focus was on monitoring any changes in liver, kidney, and heart function induced by the introduction of UPN@hydrogel. Additionally, we meticulously studied the inflammatory response prompted by the hydrogel application. We tested liver function indicators including alkaline phosphatase (ALP), albumin (ALB), and total bilirubin (TBIL) (Fig. 7B–D). Renal function indicators included urea (UREA), uric acid (UA), and creatinine (CREA) (Fig. 7E–G). Cardiac function indicators included lactate dehydrogenase (LDH), creatine kinase (CK), and creatine kinase isoenzyme (CK-MB) (Fig. 7H–J). The results showed that liver/kidney/heart function after treatments was within normal limits. The inflammatory factors we tested included IL-6, CXC10, IFN-r (Fig. 7K-M). Observation of the active status of macrophages at 0, 48 and 72 h with 800 μg/ml UP and UPN, under the microscope, which showed that the cells were in good condition, indicating that UP and UPN were not significantly toxic (Figure S7 A-C). Subsequently, CCK-8 was used to detect the viability of BMDMs and BMSCs after incubation with UPN@hydrogel at concentrations of 0–800 μg/ml for 0, 48 and 72 h, and the results showed that UPNs had no effect on the activity of the cells (Figure S7 D-F).

3. Discussion

It is crucial to continue exploring immunomodulatory molecules and biomaterials that can alter the polarization state of macrophages and establish an immune microenvironment conducive to bone regeneration [19]. Additionally, recent studies have demonstrated that M2-type macrophages can secrete cytokines and exosomes that help to regulate the osteogenic differentiation of BMSCs [20]. Improving the immune microenvironment that facilitates osteogenic differentiation of BMSCs is essential for bone defect regeneration. ECM proteins play a crucial role

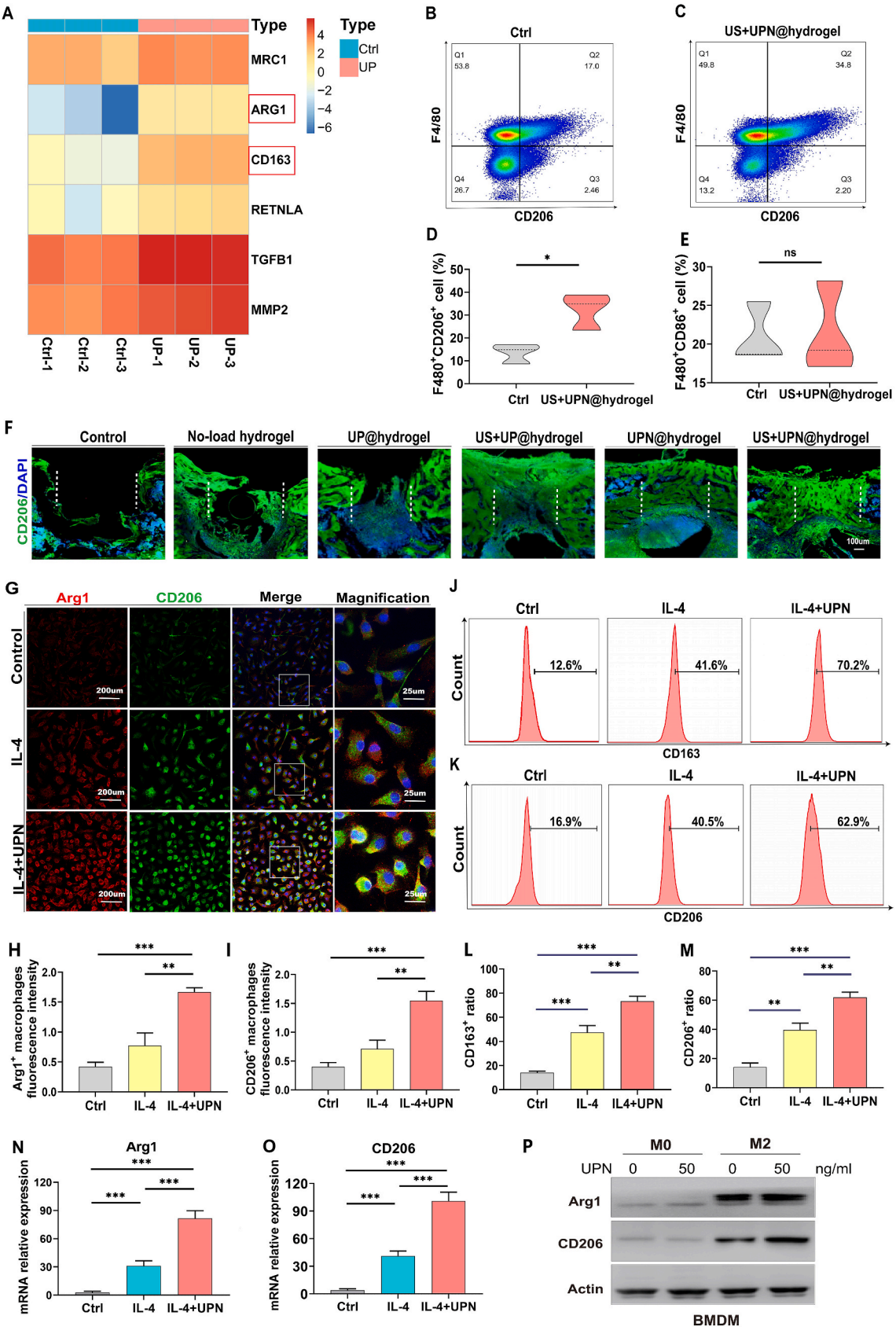

(caption on next page)

Fig. 3. Polarization of M2-type macrophages induced by UPNs. (A) Transcriptome sequencing analysis. After UP treatment in mice, the M2-type macrophage markers Arg1 and CD163 were noticeably increased. (B–C) After UPN@hydrogel with ultrasound treatment in bone defects, flow cytometry was applied to detect F4/80 and CD206 labeled M2-type macrophages, F4/80 and CD86 labeled M1-type macrophages. (D) Quantitative analysis of the difference in M2-type macrophages by flow cytometry. n = 4. (E) There was no difference in the quantification of M1-type macrophages by flow cytometry. n = 4. (F) Immunofluorescence detection of the M2-type macrophage marker CD206 in differently treated bone defects. (G–I) Immunofluorescence analysis of the M2-type macrophage markers Arg1 and CD206 in the IL-4 and IL-4+UPN groups, n = 3. (J–M) Macrophages were incubated with IL-4 and UPNs, and the M2-type macrophage markers CD163 and CD206 were quantitatively analyzed by flow cytometry, n = 3. (N–O) Macrophages were incubated with IL-4 and UPNs, and real-time PCR analysis showed that the M2-type macrophage genes Arg1 and CD206 were obviously upregulated after UPNs incubation. (P) Following treatment with IL-4 and UPN, western blots showed that UPNs promoted further upregulation of Arg1 and CD206 in macrophages. Quantitative data for cell experiments are shown as the mean ± SD (n = 3). *: $P < 0.05$; **: $P < 0.01$; ***$p < 0.001$.

in osteoblast differentiation and bone regeneration [21]. Dentin matrix protein 1 (DMP1) is a key ECM protein highly expressed in bone that regulates bone mineralization [22]. In a genetic mouse model with a DMP1 gene mutation, gene transcriptome sequencing analysis results showed that loss of DMP1 is closely related to changes in immune signaling pathways in bone [23]. Interestingly, the DMP1 amino acid sequence is rich in amino acids S or E, with an S:E ratio close to 3:2. To promote BMSC differentiation in an osteoporosis model, we designed and synthesized the ultrashort peptide SESSE [24]. Recently, our research has revealed a significant finding indicating that DMP1 and its derivative peptides, including SESSE, had the capacity to modulate M2-type macrophage polarization (unpublished data). However, it remains unknown whether SESSE peptide can effectively regulate the immune microenvironment to promote bone regeneration. Furthermore, the limited stability and longevity of SESSE posed challenges to its clinical translational outcomes. These discoveries highlighted the need for further investigation in order to determine the therapeutic potential of SESSE in promoting bone regeneration and address the stability issues for successful clinical application.

In this study, we have developed a novel approach to enhance the *in vivo* stability of ultrashort peptides (UPs) by employing a modular supramolecular self-assembly concept. Specifically, we designed a peptide called SESSE, which possessed the ability to undergo self-assembly and form supramolecular assemblies known as UPNs (Ultrashort Peptide Nanofibers). The formation of UPNs significantly improved the stability and longevity of SESSE peptides within the biological environment. The self-assembled peptide nanofiber monomer comprises two functional domains: (1) the self-assembly domain CFF, derived from β amyloid peptides to form a peptide sequence and provide crosslinking sites; [24] and (2) the therapeutic domain SESSE. In aqueous conditions, the hydrophobic action and π-π stacking of the FF domain cause the peptide monomer's self-assembly into nanofibers, with the FF domain forming a hydrophobic core and the SESSE peptide domain forming a hydrophilic core with a negative charge [25]. In this study, our primary objective was to create a favorable microenvironment that promoted immune response during the early stages of bone injury recovery, thus facilitating the differentiation of bone marrow-derived mesenchymal stem cells (BMSCs). To achieve this, we proposed the utilization of an ultrasound-controlled hydrogel system for controlled release of highly concentrated bioactive oligopeptides during the initial phase of injury. Essentially, our investigation revolved around elucidating the short-term immunomodulatory effects and stem cell differentiating properties. Consequently, the hydrogel employed in this study did not necessitate substantial mechanical strength or long-term durability for osteogenesis. However, future improvements in the biomechanical properties and resilience of this hydrogel could hold promising prospects in long-term applications.

The mechanisms of such ultrashort peptides achieve immunomodulation have not been clearly elucidated in previous studies [10a]. Macrophages are activated by metabolic reprogramming, which plays a crucial role in immunomodulation during bone regeneration[[4a,8, 10]]. Mitochondria function as coordinators of the immune response, regulating the metabolic balance of macrophages and closely affecting macrophage phenotype [26]. This study found that UPN@hydrogel regulated macrophage polarization into the M2 phenotype by activating mitochondrial functions. JC-1 is produced by the accumulation of matrix metalloproteinases (MMPs) in mitochondria. Furthermore, UPN stimulation significantly enhanced the signal of aggregates for the mitochondrial membrane potential marker JC-1, increased adenosine triphosphate release from mitochondria, and reduced the release rate of mitochondrial ROS free radicals. Therefore, we hypothesize that mitochondria may transmit signals and provide energy in the form of metabolites to maintain the macrophage phenotype.

Mitochondria, as signal organelles, are considered to be the main bioenergetic organelles that provide energy for cellular activity and are involved in the dynamic regulation of cell-specific phenotypes [27]. More importantly, mitochondrial metabolites provide signals in the induction and maintenance of macrophage polarization, and play an important role as early checkpoint molecules [28]. This study showed that UPN@hydrogel induced the TCA cycle and glycolytic metabolism in macrophages, and its metabolites were essential for macrophage polarization. Succinate is a pro-inflammatory metabolite in the TCA cycle that accumulates in lipopolysaccharide induced M1 macrophages [15a]. We found that UPN@hydrogel resulted in an obviously reduction of pro-inflammatory succinate in macrophages. Lactic acid and glucose 6 phosphate are pro-inflammatory products of glycolysis [29], UPN@hydrogel attenuated the production of inflammatory metabolites in macrophage energy metabolism. Collectively, UPN@hydrogel promoted anti-inflammatory metabolites and inhibited pro-inflammatory metabolites in the TCA cycle and glycolysis of macrophages, which may promote M2-type macrophage polarization. Moreover, our investigation unveiled that UPNs exhibited an additional capability to modulate the polarization of M2-type macrophages through the STAT6/P-PAR-γ/SOCS3 signaling pathway. Specifically, interleukin-4 (IL-4) activation triggered the transcription factor STAT6, which assembled into an activated transcriptional activator and binded to specific target genes, thereby facilitating the induction of PPAR-γ heterodimerization and subsequent activation of M2 macrophages. Furthermore, STAT6 inhibited the expression of SOCS3, thus promoting the polarization of M2-type macrophages [30]. The findings from our study provided substantial evidence supporting the notion that UPNs exerted regulatory effects on M2-type macrophage polarization via the STAT6/P-PAR-γ/SOCS3 signaling pathway.

To elucidate the intricate interplay between UPN-induced M2-type macrophages and BMSCs, we devised a sophisticated coculture system involving bone marrow-derived macrophages (BMDMs) and BMSCs. The obtained results unequivocally demonstrated that UPN-induced M2-type macrophages profoundly augmented the secretion of growth factors BMP2 and IGF-1 in the coculture microenvironment. This augmentation, in turn, significantly enhanced the osteogenic differentiation and migratory capacity of BMSCs, thereby offering new insights into the potential role of UPN-induced M2-type macrophages in promoting bone regeneration. Although our previous study demonstrated that SESSE directly promoted BMSC osteogenic differentiation, prolonged exposure for more than eight weeks was needed. In addition, ultrasound was used to control SESSE release. During the early stage of bone repair, immune cells play critical roles whereas BMSC osteogenic activity usually occurs later than three days. Furthermore, it is noteworthy that within the *in vitro* setting, UPNs at stimulation concentrations ranging from 10 to 200 ng/ml displayed a remarkable resilience

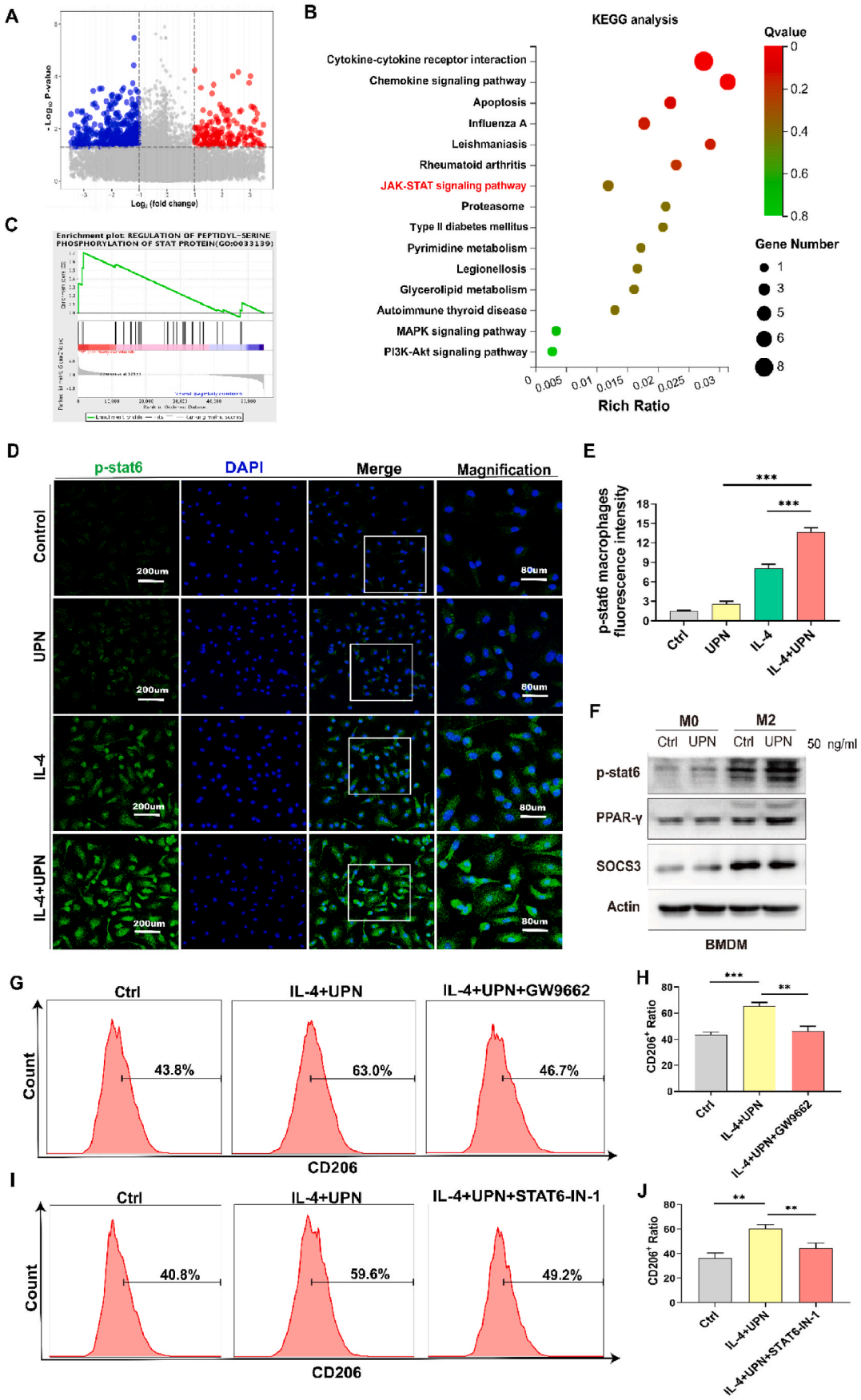

(caption on next page)

Fig. 4. The STAT6-PPAR-γ-SOCS3 signaling pathways to regulate macrophage polarization induced by UPNs. (A–C) Transcriptome sequencing analysis showed that bone defects in mice were closely associated with the JAK-STAT signaling axis of M2 type macrophages after UPN treatment. (D–E) Immunofluorescence showed that UPNs significantly enhanced bone marrow-derived M2 type macrophage p-STAT6 expression. (F) Quantitative analysis of western blots. UPNs obviously enhanced the protein content of p-STAT6 and PPAR-γ in bone marrow-derived M2 type macrophages and reduced the protein expression of SOCS3. (G–H) Flow cytometry detection of GW9662 (PPAR-γ inhibitor) inhibited IL-4 and UPN induced expression of the M2 type macrophage marker CD206. (I–J) Flow cytometry detection of STAT6-IN-1 (p-STAT6 inhibitor) inhibited IL-4 and UPN induced expression of the M2 type macrophage marker CD206. Quantitative data for cell experiments are shown as the mean ± SD (n = 3). **: P < 0.01; ***p < 0.001.

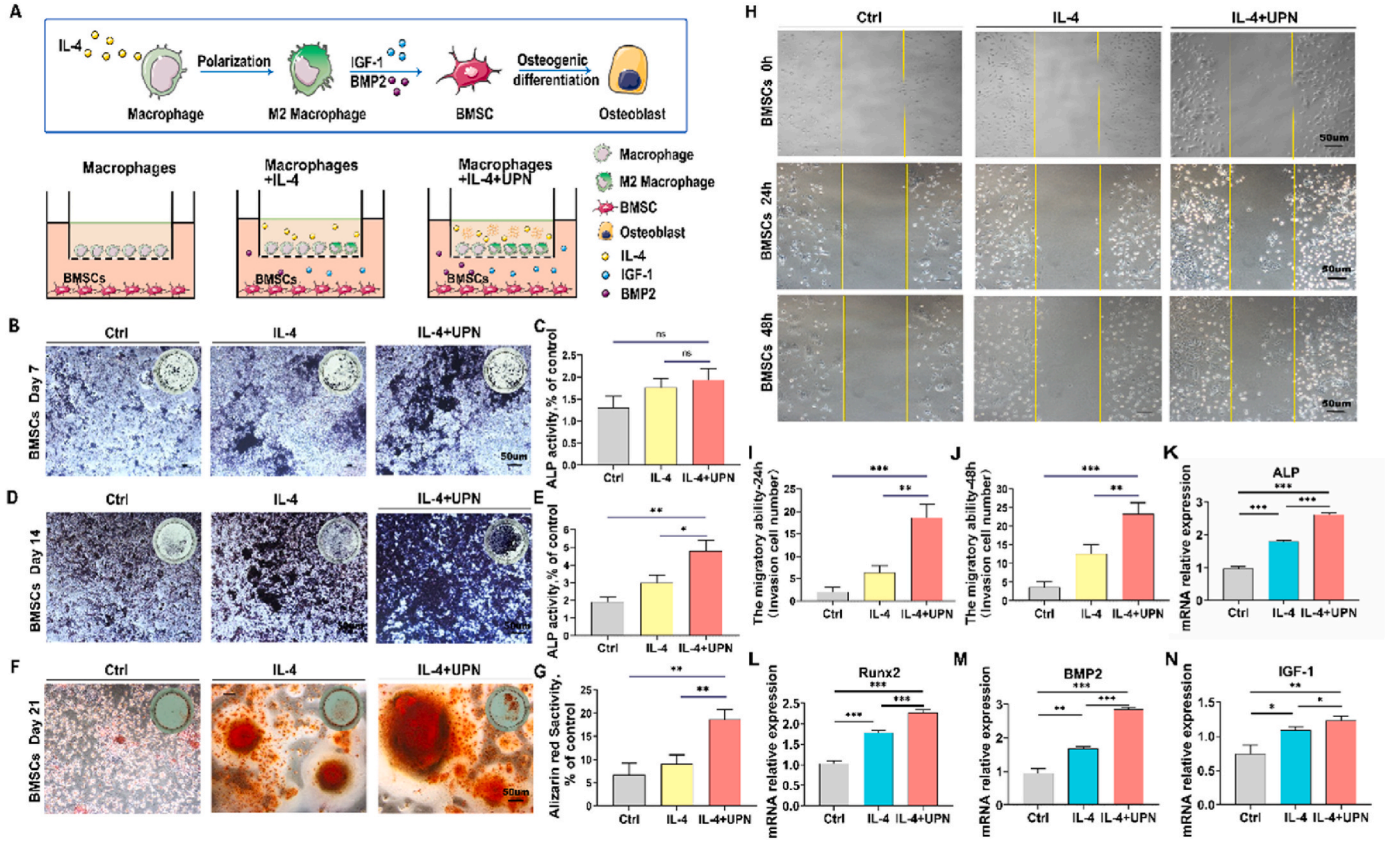

Fig. 5. Promoting the osteogenic differentiation and migration of bone marrow BMSCs by UPNs. (A) Schematic illustration of BMSC coculture with UPN-treated macrophages. (B–C) In the coculture system, alkaline phosphatase was used to detect the degree of osteogenic mineralization of BMSCs. On day 7, there was no significant difference. (D–E) On day 14, UPNs further promoted the osteogenic mineralization capacity of BMSCs compared to that of the Ctrl group and the IL-4 group. (F–G) In the coculture system, alizarin red S calcium staining was performed to detect the osteogenic mineralization of BMSCs on day 21. (H–J) In the coculture system, a migration experiment was performed to determine the migration capacity of BMSCs at 0, 24, and 48 h. (K–L) RT–qPCR to quantitatively detect the osteogenesis markers ALP and Runx2 in BMSCs. (M–N) RT–qPCR to quantitatively detect the cell growth factors BMP2 and IGF-1 secreted by M2 type macrophages. Quantitative data for cell experiments are shown as the mean ± SD (n = 3). *: P < 0.05; **: P < 0.01; ***p < 0.001. Bar = 50 μm.

against engulfment by BMSCs over a time span of 6–24 h. This intriguing observation leaded us to hypothesize that the primary mechanism by which the SESSE hydrogel governed BMSC differentiation was through indirect regulation via immune cell modulation. By influencing the immune cell population, the SESSE hydrogel potentially orchestrated a favorable microenvironment that promoted BMSC differentiation and subsequent bone regeneration.

To evaluate the efficacy of ultrasound-triggered UPN@hydrogel in promoting bone regeneration, we established a bone defect model using 8-week-old C57BL/6J mice. Subsequently, the created bone defect was treated with ultrasound-triggered UPN@hydrogel, enabling us to assess its therapeutic potential in facilitating bone repair. At 14 days after surgery, results showed that the US + UPN@hydrogel group had a better bone healing effect. Moreover, comprehensive biological analysis demonstrated that the US + UPN@hydrogel group exhibited the highest levels of bone morphogenetic protein 2 (BMP2) and collagen type I (Col1), mirroring the findings obtained from our *in vitro* investigations. Histological examination using hematoxylin and eosin (H&E) staining revealed a gradual replacement of newly formed trabeculae by regenerated bone within the bone defect region of mice. Immunofluorescence detection targeting the osteogenesis gene marker BMP2 exhibited intense red fluorescence, with the US + UPN@hydrogel group displaying the most robust fluorescence intensity as compared to the control (Ctrl) group. These results collectively indicated that the ultrasound therapy administered from days 1–3 following the onset of bone defect modeling effectively induced the conversion of macrophages into the M2 subtype, thereby significantly altering the immune microenvironment surrounding the site of bone injury, ultimately augmenting the healing process of the bone defect. Importantly, the application of ultrasound also facilitated the release of self-assembled peptides from the hydrogel due to ultrasonic acceleration, consequently promoting osteogenesis and substantially enhancing the reparative capacity of the bone defects.

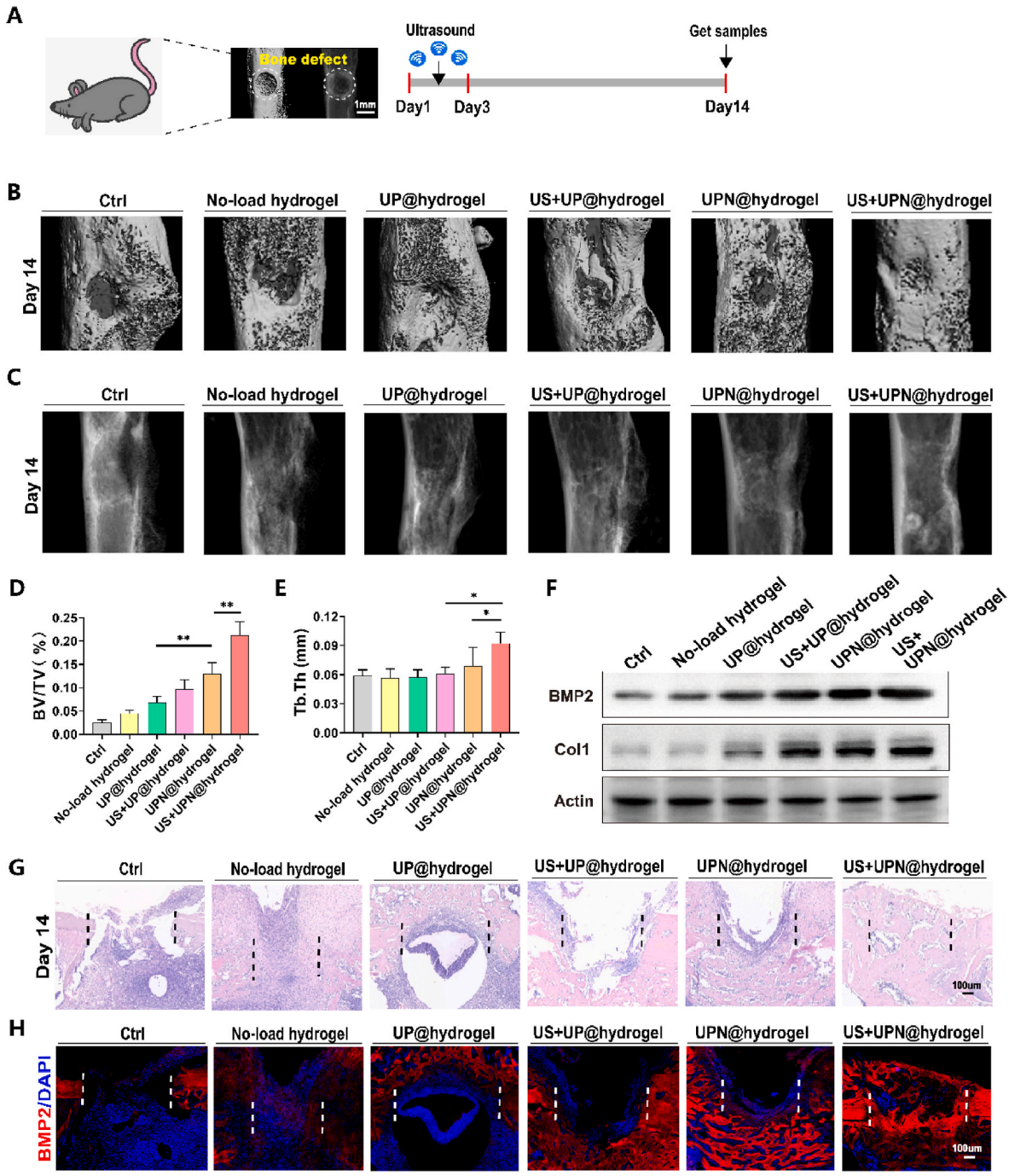

Fig. 6. Ultrasound-responsive UPN@hydrogel promotes bone defect regeneration in mice. (A) *In vivo* mouse femoral bone defect model with ultrasound treatment administered during days 1–3 of bone healing (ultrasound parameters: power: 1.75 W/cm2, frequency: 1 MHz, ultrasound duration: 2 min per treatment). (B) Micro-computed tomography (micro-CT) reconstruction depicting the bone defect site on postoperative day 14 (n = 5). (C) X-ray image illustrating the bone defect site on day 14 after surgery (n = 5). (D–E) Quantitative assessment of micro-CT parameters within the healing region of bone defects, including BV/TV (relative bone volume fraction in the area of bone defect healing) and Tb/Th (trabecular thickness of the defect area). (F) Western blot analysis of the bone defect site on postoperative day 14. (G) Hematoxylin and eosin (H&E) staining of mouse bone defect areas (scale bar = 100 μm). (H) Immunofluorescence staining to detect osteogenesis in different experimental groups. Bar = 100 μm *: $P < 0.05$; **: $P < 0.01$. n = 6.

4. Conclusion

We have developed an ultrasound-triggered peptide nanofiber hydrogel to effectively promote bone regeneration. The ultrashort peptide SESSE was designed with modules for M2 macrophage polarization and self-assembly to alter the macrophage state. The released peptide nanofibers activated oxidative stress in macrophage mitochondria, which in turn inhibited reactive oxygen species release while also inducing M2 macrophages to accelerate the osteogenic differentiation of bone marrow mesenchymal stem cells. In summary, this study provides a novel avenue for active ultrashort peptide-based tissue engineering wherein bioactive materials based on ultrashort peptides can be designed to promote tissue damage regeneration.

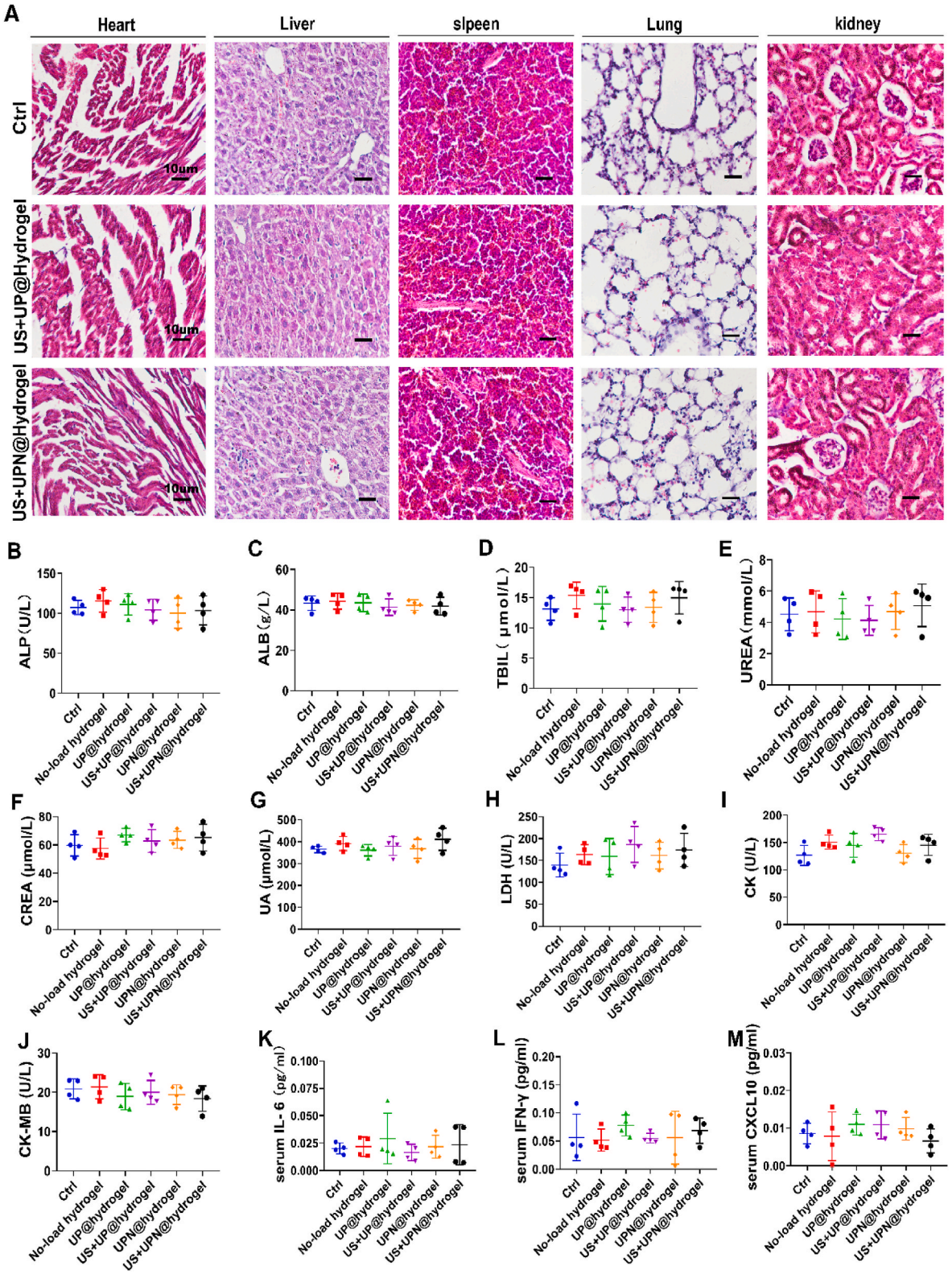

Fig. 7. ***In vivo*** **toxicity study of UPNs.** (A) H&E staining to detect toxicity in the heart, liver, spleen, lungs and kidneys after treatment with the US + UP@hydrogel and US + UPN@hydrogel for 14 days. Bar = 10 μm. (B–D) Biochemical parameters of liver function including alkaline phosphatase (ALP), albumin (ALB), and total bilirubin (TBIL). (E–G) Biochemical parameters of renal function including urea (UREA), uric acid (UA), and creatinine (CREA). (H–J) Biochemical parameters of cardiac function including lactate dehydrogenase (LDH), creatine kinase (CK), and creatine kinase isoenzyme (CK-MB). (K–M) Inflammatory indicators in the serum of the different treatment groups including IL-6, CXC10, and IFN-r.

5. Experimental section/methods

5.1. Preparation of ultrashort peptide nanofibers

A fresh stock solution of CFFSESSE peptide was prepared by dissolving the lyophilized form of the peptide in dimethyl sulfoxide (DMSO) at a concentration of 10.0 mg/ml for each experiment to avoid preaggregation. Then, 0.5 ml of the peptide stock solution was added dropwise into 2.0 ml deionized water solution and allowed to stand for 5 min. The mixture then underwent shaking for another 12 h to obtain self-assembled ultrashort peptide nanofibers. Finally, the organic solvent was removed by dialysis against deionized water for 2 days. The as-prepared ultrashort peptide nanofibers were lyophilized for storage.

5.2. Preparation of ultrasound-responsive hydrogels loaded with peptide nanofibers

For peptide nanofiber loading into the hydrogel, 5.0 mg of the as-prepared peptide nanofiber was premixed with 1 ml of 2.5% (*w/v*) sodium alginate, which was then added to 1.0 ml of 0.1 M calcium chloride ($CaCl_2$) solution and allowed to stand for 10 min. The peptide nanofiber-loaded hydrogel was washed with deionized water.

5.3. Morphology of the ultrashort peptide nanofibers

The morphology of the ultrashort peptide nanofibers was evaluated with scanning electron microscopy (Zeiss Sigma 300 VP instrument). The characteristics were noted twice using electronic mode at 2 kV.

5.4. Properties of the ultrashort peptide nanofibers

5.4.1. Ultraviolet–vis spectrum

The ultraviolet–visible absorbance spectrum was measured using an ultraviolet–vis spectrophotometer (INESA, China) at 25 °C. The wavelength range was set at 200–650 nm, and the scanning speed was medium.

5.4.2. Modulus

Rheological analysis of the calcium alginate hydrogel was performed using a HAKKE rheometer. The viscoelasticity of the hydrogel was measured using strain sweep experiments under oscillation conditions. The scan tested the strain from 0.1% to 10% to record the storage modulus (G') and loss modulus (G'') values. Different samples were used as replicates for all runs. The frequency used was 1 Hz, and the gap width was 5 mm.

5.4.3. Hydrogel degradation and ultrasound-responsive degradation

Following gelatinization, the hydrogel was carefully weighed (W0) at a temperature of 37 °C. Subsequently, it was immersed in phosphate-buffered saline (PBS) with a pH value of 7.4 to create an appropriate physiologically relevant environment. Then, the external water was removed from the sample, and the samples were weighed (WS) at specific intervals. All experiments were performed in triplicate. For ultrasound-responsive degradation experiments, samples were treated using ultrasound at intervals (20 kHz, 45 W, 3 min). In the above experiments, all the samples were weighed after external water was removed.

5.4.4. Peptide release and ultrasound-responsive release

The hydrogel-releasing peptides were analyzed with or without ultrasound irradiation. The hydrogel containing the peptide was immersed in 5.0 ml PBS buffer (pH 7.4). After a preset time interval, 1.0 ml of solution was collected from the mixture solution, and the same volume of fresh PBS was added. The concentration of peptides was then analyzed using a fluorescence spectrophotometer. In ultrasound-stimulated peptide release experiments, samples were irradiated at specific intervals using ultrasound (20 kHz, 45 W, 3 min). Then, 1.0 ml of solution was extracted and analyzed using a fluorescence spectrophotometer.

5.5. Construction of a mouse femoral defect model

This experiment was approved by the Medical Ethics Committee of the School of Stomatology of Tongji University (2019-DW-040). A total of 36 male C57BL/6J mice, aged 8 weeks, were used in this study. Mice were housed under specific pathogen-free (SPF) conditions with controlled temperature (22 ± 1 °C) and humidity (40%–60%) and a 12 h light/dark cycle, and provided food and water. Surgical instruments were sterilized by autoclaving before surgery, and 10% chloral hydrate (3 ml/kg) was injected intravenously. After the mice were anesthetized, they were moved to the experimental bench and disinfected with 3% iodine tincture solution and 75% alcohol at the surgical site. Following this, the skin at the femur of the mouse was incised, the muscles and fascia were bluntly peeled off, the femur was exposed, a 0.8 mm diameter spherical drill was used to penetrate the bone cortex on one side, and the ultrashort peptide nanofiber hydrogel was immediately placed locally at the site of the bone defect. The skin was then sutured with absorbable 4–0 filaments, thereby constructing a femur injury repair model. After surgery, antibiotics were used to control the infection, and an electric mattress (38.3 ± 0.5) °C was used to keep the animal warm. After the animal was fully awakened from anesthesia, it was returned to the appropriate cage. After bone defect surgery in mice, a medical couplant was applied at the site of the defect for the first three days, and ultrasound treatment was performed for 2 min at 1.75 W/cm^2 watts per square meter (1 M/Hz). The mice in this experiment were divided into six groups: (1) **Ctrl group**: group without any treatment (denoted as "Control group"); (2) **Unloaded hydrogel group**: unloaded calcium alginate hydrogel (denoted as "Unloaded hydrogel group"); (3) **UP@hydrogel group**: ultrashort peptide-loaded calcium alginate hydrogel (denoted as "UP@hydrogel group"); (4) **US + UP@hydrogel group**: ultrasound treatment + ultrashort peptide-loaded calcium alginate hydrogel (denoted as "US + UP@hydrogel group"); (5) **UPN@hydrogel group**: ultrashort peptide nanofiber-loaded calcium alginate hydrogel (denoted as "UPN@hydrogel group"); and (6) **US + UPN@hydrogel group**: ultrasound treatment + ultrashort peptide nanofiber-loaded calcium alginate hydrogel (denoted as "US + UPN@hydrogel group"). Each group contained six experimental mice.

5.6. Microcomputed tomography (CT) assay for bone defect repair

A total of 36 mice in the control and experimental groups were euthanized 14 days after femur injury. Bone defect samples were analyzed using a micro-CT system (micro-CT50, Switzerland). Briefly, each sample was scanned for 80 layers from the bone defect, including the entire bone injury area, and the bone density of all bone trabeculae in the selected area, with a spatial voxel size of 10 μm, was quantified at 70 kV and 200 mA. Furthermore, the following bone density parameters were regenerated from micro-CT analysis: trabecular volume/total volume (BV/TV) and bone trabecular thickness (Tb.Th).

5.7. Biological assays

5.7.1. Isolation and culture of mouse bone marrow-derived mesenchymal stem cells (BMSCs)

After painless euthanasia of 36 SPF-grade 4-week-old C57BL/6J mice, the mice were soaked in 75% ethanol for 10 min. The skin was incised at the femur and tibia, followed by sterile separation of the femur, and soaking in a sterile PBS solution containing penicillin–streptomycin. Then, the muscles and connective tissue around the femur and tibia were removed and washed thrice in a double antibacterial PBS solution. Next, both ends of the femur and tibia were cut, exposing the bone marrow cavity. The sample was rinsed thrice with a 2

ml syringe using complete culture solution. Moreover, the bone marrow chamber was rinsed several times until the bone wall color turned white. The cell suspension was then passed through a 200-mesh nylon mesh to a 15 ml centrifuge tube and centrifuged at 2000 rpm for 5 min. The supernatant was discarded, and the cells were resuspended with erythrocyte lysate and lysed at 4 °C for 10 min. An equal amount of medium was added to stop erythrocyte lysis, and then the sample was centrifuged at 2000 rpm for 5 min. The cells were counted, inoculated onto a 10 cm Petri dish, and cultured at 37 °C and 5% CO_2 with saturated humidity.

5.7.2. Isolation of mouse bone marrow-derived macrophages (BMDMs)

The process for extracting cells from mouse bone marrow chambers was similar to that used for mouse bone marrow mesenchymal stem cells until the erythrocytes were lysed, and then the cells were resuspended in M-CSF medium (40 ng/ml) (recombinant mouse M-CSF; Petroleum Technology, Rocky Mountain, NJ). The culture medium containing M-CSF was replenished on days 2 and 3, and fresh M-CSF culture medium was added on day 5. This *in vitro* experiment included four groups: (1) **Ctrl group**: group without any treatment (denoted as the "Control group"); (2) **IL-4 group**: macrophages were induced with IL-4 (denoted as the "IL-4 group"); (3) **UPN group**: macrophages were induced with ultrashort peptide nanofibers (denoted as the "UPN group"); (4) **IL-4+UPN** group: macrophages were induced with IL-4 and ultrashort peptide nanofibers (denoted as the "IL-4+UPN group").

5.7.3. Immunofluorescence

Immunofluorescence staining was used to detect macrophage polarization and stem cell osteogenic capacity. The six groups were euthanized 14 days after bone injury treatment, and the femurs with the bone defects were collected and fixed with 4% paraformaldehyde. After fixation for 48 h, the collected tissues were placed in 10% EDTA for 4 weeks, with replacement of the decalcification solution every two days. The decalcified specimens were then washed with PBS, dehydrated with 30% sucrose solution for 48 h and immersed in Tissue-Tek® O·C.T. for embedding. The bone defect was cut continuously using a cryostat (Leica Microsystems, Germany) with a uniform thickness of 4 μm per layer. After the cut sample was placed at room temperature for 30 min, it was then placed in acetone at 4 °C for 10 min. Next, it was oven dried for 30 min and washed thrice with PBS for 5 min. Subsequently, immunofluorescence staining was performed after blocking the sections with 10% goat serum at room temperature for 1 h. PBS diluted with appropriate proportions of primary antibody working solution (BMP2, 1:200, Bioss) was added dropwise to the sample and incubated overnight at 4 °C in a dark environment. Drip washes with PBS were carried out thrice, each for 10 min, and then an appropriate dilution of the secondary antibody working solution and mouse-derived antibody (594, 1:1000, Thermo Fisher) was added. Under a confocal microscope (NIS Elements, Nikon, Japan), analysis was carried out using specialized image software (ImageJ, NIH, USA).

To evaluate cell migration, cells were fixed in 4% paraformaldehyde for 20 min at room temperature, washed in PBS and then blocked in 10% goat serum for 1 h. The cells were washed again with PBS 3 times for 5 min each. PBS diluted with appropriate proportions of primary antibody working solution (Arg1, 1:200, Bioss; CD206, 1:200, Proteintech; p-stat6, 1:100, Cell Signal) was added dropwise to the sample and incubated overnight at 4 °C in a dark environment. Under a confocal microscope (NIS Elements, Nikon, Japan), analysis was carried out using specialist image software (ImageJ, NIH, USA).

5.7.4. Western blotting

Prechilled lysis buffer was added to the cells; however, 50 μl protease inhibitors and 50 μl phosphatase inhibitors were added to the cells before lysis. Next, 250 μl of WB Super RIPA lysis buffer was added to 1×10^6 cells, and 2.5 μl each of protease inhibitor and phosphatase inhibitor mixture was added. The mixture was left on ice to lyse the cells for 30 min and then centrifuged at 4 °C for 5 min at 13,000 rpm. The supernatant was collected, which contained the protein that needed to be extracted. The protein content was determined using the BCA technique, and the concentration of the obtained sample was calculated. After mixing with the appropriate buffer, a 5 × sodium dodecyl sulfate (SDS) gel was heated at 70 °C for 10 min for denaturation. Protein extracts were effectively isolated using SDS–PAGE and PVDF membranes, which were saturated with pure methanol for 5 s. Protein blocking was performed with a fast-blocking solution (Biotech, NO. C510053), and the samples were incubated overnight at 4 °C with a diluted primary antibody. TBST (Biotech, No. C006161) was used to wash the PVDF membrane thrice for 10 min. Then, diluted secondary antibody was added, and the membrane was incubated for 1 h. PVDF film development was performed using a chemiluminescent kit (Pierce, USA). The primary antibody working solutions were as follows: BMP2, 1:1000 (Bioss, China); Col1, 1:1000 (Bioss, China); Arg1, 1:1000 (Bioss, China); and CD206, 1:1000 (Proteintech, USA). The secondary antibody working solutions were as follows: A32790, 1:1000, and A32729, 1:1000 (Thermo Fisher, China).

5.7.5. Real time quantitative polymerase chain reaction (RT–qPCR)

According to the manufacturer's instructions, RNA was extracted using TRIzol (Takara, China) reagent, and 1.0 μg of RNA was reverse transcribed to cDNA using HiScript II Q RT SuperMix. All data were based on β-actin as a unified reference based on previous studies [27]. The RT–qPCR primer sequence was as follows:

Gene	Forward Sequence (5′to3′)	Reverse Sequence (5′to3′)
β-actin	CATCCGTAAAGACCTCTAGCCAAC	ATGGAGCCACCGATCCACA
BMP2	GGGACCCGCTGTCTTCTAGT	TCAACTCAAATTCGCTGAGGAC
IGF-1	CTGGACCAGAGACCCTTTGC	GGACGGGGACTTCTGAGTCTT
RUNX2	ATGCTTCATTCGCCTCACAAA	GCACTCACTGACTCGGTTGG
ALP	CCAACTCTTTTGTGCCAGAGA	GGCTACATTGGTGTTGAGCTTTT
COL1	GAGAGCGAGGATACACTGGC	CTGGCCTTGAAATCCCTGG
Arg1	GTCTGGCAGTTGGAAGCATCT	GCATCCACCCAAATGACACA
IL-10	GCTCTTACTGACTGGCATGAG	CGCAGCTCTAGGAGCATGTG
TGF-β	CTCCCGTGGCTTCTAGTGC	GCCTTAGTTTGGACAGGATCTG
CD206	GGTGGAAGAAGAAGTAGCCT	GAAGGGTCAGTCTGTGTTTG

5.7.6. Alizarin red staining

BMSCs were seeded on 12-well plates at a density of 2×10^4 cells/ml and stained with alizarin red on day 21 when the cell density reached 80% confluence. Alizarin red staining solution (Sigma–Aldrich) was prepared according to the manufacturer's instructions by adjusting the pH to 8.3 and storing it at 4 °C for later use. PBS (Promo Cell, United Kingdom) washing was performed twice on the stained sample for 5 min. Cells within the well were fixed at room temperature using 4% paraformaldehyde for 30 min, washed with distilled water (diH_2O) thrice, stained with alizarin red staining solution for 30 min at 37 °C, washed with diH_2O and dried. Red mineralized nodules int the cells were observed under 20x magnification using an upright light microscope (Leica, United Kingdom).

5.7.7. Alkaline phosphatase activity test

After BMSCs were isolated and cultured, they were seeded into 12-well plates at a density of 6×10^4 cells/ml, and the cells were cultured for 7 and 14 days. A basic phosphatase (ALP) stain was then performed when the cell density reached 80%. Alkaline phosphatase chromogenic solution was prepared according to the manufacturer's instructions (Mlbio, Shanghai, China). PBS (PromoCell, United Kingdom) was used to rinse the sample twice for 5 min each time. Cells in the wells were fixed at room temperature with 4% paraformaldehyde for 30 min and washed thrice using diH_2O. Then, the cells were incubated at 37 °C for 30 min, washed with diH_2O and dried. The cells were photographed at 20x magnification by light microscopy (Leica, United Kingdom), with alkaline phosphatase staining appearing as a blue color.

5.7.8. Cytotoxicity testing in vitro

The UP group and UPN groups were incubated for 6 h in advance, with concentrations of 6.25 ng/ml, 12.5 ng/ml, 25 ng/ml, 50 ng/ml, 100 ng/ml and 200 ng/ml, and the culture time of cells exposed to different concentrations of active peptides was 0, 48 and 72 h. Cell proliferation was detected using a Cell Counting Kit-8 (CCK-8) based on the manufacturer's guidelines. A total of 100 μl of CCK-8 per 2 ml of medium was added and incubated for 2 h. A Gen5™ microplate reader (BioTek instrument) was used to assay the cells at 450 nm (12-well plate 3 × 3 dots). Additionally, the active state of the cells was observed under the microscope.

5.7.9. Cytotoxicity testing in vivo

In mice with bone defects, ultrashort peptide hydrogels were placed in the US + UP@hydrogel group, ultrashort peptide nanofiber hydrogels were placed in the US + UPN@hydrogel group, and both groups were treated with ultrasound. After 14 days, the heart, kidney, spleen, lungs and liver were collected for hematoxylin and eosin (H&E) staining to observe the cell structure and morphology of these organs, and the status of the mice was closely observed.

5.8. Statistical analysis

The data were presented as means±standard deviations. SPSS 19.0 software (SPSS, Chicago, IL) was used to perform statistical analysis. The Kolmogorov-Smirnov test was applied to verify the normal distribution of data. The significant effects of the variables were tested with one-way analysis of variance (ANOVA). Multiple comparison Tukey tests were utilized to compare the data at a preset alpha of 0.05. A value of $P < 0.05$ were regarded as statistically significant.

Declaration of competing interest

The authors declare no conflict of interest.

Ethics approval

All animals were bred according to the National Institutes of Health's Guide for Care and Use of Laboratory Animals. All animal studies were carried out in accordance with the guidelines of the Institutional Animal Care and Use Committees of Tongji University, and followed all ARRIVE recommendation (Animal studies:Reporting of In Vivo Experiments) guidelines.

CRediT authorship contribution statement

Fan Zhang: Conceptualization, Methodology, Validation, Investigation, Data curation, Writing – original draft, Writing – review & editing, Visualization. **Mingchen Lv:** Conceptualization, Methodology, Data curation, Writing – original draft, Writing – review & editing. **Siyuan Wang:** Methodology, Data curation. **Mengyao Li:** Methodology, Data curation. **Yu Wang:** Methodology, Data curation. **Congjiao Hu:** Methodology, Data curation. **Wei Hu:** Methodology, Data curation. **Xuekui Wang:** Methodology, Data curation. **Xiaogang Wang:** Methodology, Data curation. **Zhiduo Liu:** Methodology, Data curation. **Zhen Fan:** Conceptualization, Validation, Investigation, Writing – original draft, Writing – review & editing, Visualization, Supervision, Project administration, Funding acquisition. **Jianzhong Du:** Conceptualization, Validation, Investigation, Writing – original draft, Writing – review & editing, Visualization, Supervision, Project administration, Funding acquisition. **Yao Sun:** Conceptualization, Validation, Investigation, Writing – original draft, Writing – review & editing, Visualization, Supervision, Project administration, Funding acquisition.

Acknowledgements

This work was financially supported by National Key R&D Program of China (2022YFA1103200), National Natural Science Foundation of China (81822012, 82061130222, 81771043, 22075212, 21925505, 52222306, 22075212), Shanghai Academic Leader of Science and Technology Innovation Action Plan (20XD1424000), Innovation Program of Shanghai Municipal Education Commission (2023ZKZD28), the Shanghai Experimental Animal Research Project of Science and Technology Innovation Action Plan (8191101676, 201409006400), and Shanghai International Scientific Collaboration Fund (21520710100).

Appendix A. Supplementary data

Supplementary data to this article can be found online at https://doi.org/10.1016/j.bioactmat.2023.08.008.

References

[1] a) G.-D. Cao, Y.-Q. Pei, J. Liu, P. Li, P. Liu, X.-S. Li, Zhong Guo Gu Shang 34 (2021) 382;
b) S. Jia, A. Meng, Development (Cambridge, England), 2021, p. 148.
[2] a) Q. Chen, P. Shou, C. Zheng, M. Jiang, G. Cao, Q. Yang, J. Cao, N. Xie, T. Velletri, X. Zhang, C. Xu, L. Zhang, H. Yang, J. Hou, Y. Wang, Y. Shi, Cell Death Differ. 23 (2016) 1128;
b) Y. Xiong, B.-B. Mi, Z. Lin, Y.-Q. Hu, L. Yu, K.-K. Zha, A.C. Panayi, T. Yu, L. Chen, Z.-P. Liu, A. Patel, Q. Feng, S.-H. Zhou, G.-H. Liu, Mil. Med. Res. 9 (2022) 65.
[3] W. Hu, Y. Chen, C. Dou, S. Dong, Ann. Rheum. Dis. 80 (2021) 413.
[4] a) J. Lee, H. Byun, S.K. Madhurakkat Perikamana, S. Lee, H. Shin, Adv. Healthcare Mater. 8 (2019), e1801106;
b) K. Zheng, W. Niu, B. Lei, A.R. Boccaccini, Acta Biomater. 133 (2021) 168.
[5] a) D. Zhang, Y. Wu, Z. Li, H. Chen, S. Huang, C. Jian, A. Yu, J. Nanobiotechnol. 19 (2021) 226;
b) D. Lu, Y. Xu, Q. Liu, Q. Zhang, Front. Cell Dev. Biol. 9 (2021), 681171;
c) Q. Hou, J. Huang, H. Ayansola, H. Masatoshi, B. Zhang, Front. Immunol. 11 (2020), 623691.
[6] A. J. Boutilier, S. F. Elsawa, Int. J. Mol. Sci. 2021, 22.
[7] a) L.A.J. O'Neill, M.N. Artyomov, Nat. Rev. Immunol. 19 (2019) 273;
b) J. Kim, H.-Z. Lyu, C. Jung, K.M. Lee, S.H. Han, J.H. Lee, M. Cha, Tissue Eng. Regen. Med. 18 (2021) 387;
c) G. Tian, S. Jiang, J. Li, F. Wei, X. Li, Y. Ding, Z. Yang, Z. Sun, K. Zha, F. Wang, B. Huang, L. Peng, Q. Wang, Z. Tian, X. Yang, Z. Wang, Q. Guo, W. Guo, S. Liu, Acta Biomater. 127 (2021) 131;
d) E.A. Ross, A. Devitt, J.R. Johnson, Front. Immunol. 12 (2021), 708186.
[8] a) H. Zhou, Y. Xue, L. Dong, C. Wang, J. Mater. Chem. B 9 (2021) 3608;
b) B. Lv, N. Shen, Z. Cheng, Y. Chen, H. Ding, J. Yuan, K. Zhao, Y. Zhang, Front. Bioeng. Biotechnol. 9 (2021), 813169;
c) J. Li, X. Jiang, H. Li, M. Gelinsky, Z. Gu, Adv. Mater. 33 (2021), e2004172.
[9] M. Ni, S. Zhuo, RSC Adv. 9 (2019) 844.
[10] a) L. Wang, J. Li, Y. Xiong, Y. Wu, F. Yang, Y. Guo, Z. Chen, L. Gao, W. Deng, ACS Appl. Mater. Interfaces 13 (2021), 58329;
b) A. Ilina, V. Khavinson, N. Linkova, M. Petukhov, Int. J. Mol. Sci. (2022) 23.
[11] a) J.L. Aparicio-Collado, N. García-San-Martín, J. Molina-Mateo, C. Torregrosa Cabanilles, V. Donderis Quiles, A. Serrano-Aroca, R. Sabater I Serra, Colloids Surf. B Biointerfaces 214 (2022), 112455;
b) L. Fan, M. Duan, Z. Xie, K. Pan, X. Wang, X. Sun, Q. Wang, W. Rao, J. Liu, Small 16 (2020), e1903421.
[12] a) X. Yin, L. Yan, D. Jun Hao, S. Liu, M. Yang, B. He, Z. Liu, Int. J. Pharm. 582 (2020), 119303;
b) S. Karimi, Z. Bagher, N. Najmoddin, S. Simorgh, M. Pezeshki-Modaress, Int. J. Biol. Macromol. 167 (2021) 796.
[13] S.K. Papageorgiou, E.P. Kouvelos, E.P. Favvas, A.A. Sapalidis, G.E. Romanos, F. K. Katsaros, Carbohydr. Res. 345 (2010) 469.
[14] a) L.-N. Zhou, C.-S. Bi, L.-N. Gao, Y. An, F. Chen, F.-M. Chen, Oral Dis. 25 (2019) 265;
b) G.P. Garlet, W.V. Giannobile, J. Dent. Res. 97 (2018) 1079.
[15] a) E.L. Mills, B. Kelly, A. Logan, A.S.H. Costa, M. Varma, C.E. Bryant, P. Tourlomousis, J.H.M. Däbritz, E. Gottlieb, I. Latorre, S.C. Corr, G. McManus, D. Ryan, H.T. Jacobs, M. Szibor, R.J. Xavier, T. Braun, C. Frezza, M.P. Murphy, L. A. O'Neill, Cell (2016) 167;
b) W.K.E. Ip, N. Hoshi, D.S. Shouval, S. Snapper, R. Medzhitov, Science 356 (2017) 513.
[16] Y. Shi, X. Kang, Y. Wang, X. Bian, G. He, M. Zhou, K. Tang, Med. Sci. Mon. Int. Med. J. Exp. Clin. Res. : Int. Med. J. Exp. Clin. Res. 26 (2020), e923328.
[17] B.N. Brown, B.D. Ratner, S.B. Goodman, S. Amar, S.F. Badylak, Biomaterials 33 (2012) 3792.
[18] S. Wang, H. Jiang, C. Zheng, M. Gu, X. Zheng, BMC Cancer 22 (2022) 34.
[19] A. Lockhart, D. Mucida, R. Parsa, Immunity 55 (2022) 800.
[20] J. Pajarinen, T. Lin, E. Gibon, Y. Kohno, M. Maruyama, K. Nathan, L. Lu, Z. Yao, S. B. Goodman, Biomaterials 196 (2019) 80.

[21] a) Y. Li, L. Liu, S. Li, H. Sun, Y. Zhang, Z. Duan, D. Wang, J. Bone Miner. Metabol. (2022) 40;
b) Y. Zhang, T. Böse, R.E. Unger, J.A. Jansen, C.J. Kirkpatrick, J.J.J.P. van den Beucken, Cell Tissue Res. 369 (2017) 273;
c) M. Zheng, M. Weng, X. Zhang, R. Li, Q. Tong, Z. Chen, Biomed. Mater. (Bristol, U. K.) 16 (2021), 025005;
d) G. Shen, H. Ren, Q. Shang, W. Zhao, Z. Zhang, X. Yu, K. Tang, J. Tang, Z. Yang, D. Liang, X. Jiang, EBioMedicine 52 (2020), 102626;
e) W. Lin, Q. Li, D. Zhang, X. Zhang, X. Qi, Q. Wang, Y. Chen, C. Liu, H. Li, S. Zhang, Y. Wang, B. Shao, L. Zhang, Q. Yuan, Bone Res 9 (2021) 17;
f) Y. Song, H. Wu, Y. Gao, J. Li, K. Lin, B. Liu, X. Lei, P. Cheng, S. Zhang, Y. Wang, J. Sun, L. Bi, G. Pei, ACS Appl. Mater. Interfaces 12 (2020), 16058.
[22] Y. Zhang, X. Li, Z. Luo, L. Ma, S. Zhu, Z. Wang, J. Wen, S. Cheng, W. Gu, Q. Lian, X. Zhao, W. Fan, Z. Ling, J. Ye, S. Zheng, D. Li, H. Wang, J. Liu, B. Sun, Proc. Natl. Acad. Sci. U. S. A. 117 (2020) 3083.
[23] a) A. Marahleh, H. Kitaura, F. Ohori, A. Kishikawa, S. Ogawa, W.-R. Shen, J. Qi, T. Noguchi, Y. Nara, I. Mizoguchi, Front. Immunol. 10 (2019) 2925;
b) J.Q. Feng, L.M. Ward, S. Liu, Y. Lu, Y. Xie, B. Yuan, X. Yu, F. Rauch, S.I. Davis, S. Zhang, H. Rios, M.K. Drezner, L.D. Quarles, L.F. Bonewald, K.E. White, Nat. Genet. 38 (2006) 1310.
[24] M. Cai, B. Xiao, F. Jin, X. Xu, Y. Hua, J. Li, P. Niu, M. Liu, J. Wu, R. Yue, Y. Zhang, Z. Wang, Y. Zhang, X. Wang, Y. Sun, Bone Res 10 (2022) 23.
[25] X. Yan, P. Zhu, J. Li, Chem. Soc. Rev. 39 (2010) 1877.
[26] a) M. Locati, G. Curtale, A. Mantovani, Ann. Rev. Pathol. 15 (2020) 123;
b) I. Kourtzelis, J. Hewitson, T. Roger, Front. Immunol. 12 (2021), 823023;
c) M.M. Ahamada, Y. Jia, X. Wu, Front. Immunol. 12 (2021), 734008.
[27] N.S. Chandel, Cell Metabol. 22 (2015) 204.
[28] a) I. Martínez-Reyes, N.S. Chandel, Nat. Commun. 11 (2020) 102;
b) J.T. Noe, R.A. Mitchell, J. Leukoc. Biol. 106 (2019) 359.
[29] a) D.C. Macias-Ceja, D. Ortiz-Masiá, P. Salvador, L. Gisbert-Ferrándiz, C. Hernández, M. Hausmann, G. Rogler, J.V. Esplugues, J. Hinojosa, R. Alós, F. Navarro, J. Cosin-Roger, S. Calatayud, M.D. Barrachina, Mucosal Immunol. 12 (2019) 178;
b) X. Li, M. Mao, Y. Zhang, K. Yu, W. Zhu, Biomolecules 9 (2019);
c) A. Koperniku, A.A. Garcia, D. Mochly-Rosen, J. Med. Chem. 65 (2022) 4403.
[30] a) J. Chu, X.-C. Hu, C.-C. Li, T.-Y. Li, H.-W. Fan, G.-Q. Jiang, Cell. Signal. 92 (2022), 110242;
b) W. Liu, Q. Long, W. Zhang, D. Zeng, B. Hu, S. Liu, L. Chen, Aging (Albany NY) 13 (2021), 19760.